A Wavelet-based Approach for Ball Grid Array (BGA) Substrate Conduct Paths Inspection

C. H. Yeh and D. M. Tsai
Machine Vision Lab.
Department of Industrial Engineering and Management
Yuan-Ze University, Chung-Li, Taiwan, R.O.C.
E-mail: iedmtsai@saturn.yzu.edu.tw

Abstract

The aim of this paper is to locate the boundary defects such as open, short, mousebite, and spur on Ball Grid Array (BGA) substrate conduct paths using machine vision. The 2-D boundaries of BGA substrate conduct paths are initially represented by the 1-D tangent angles. The tangent angles are evaluated from the covariance matrix eigenvector over a region of support on a boundary segment. Boundary defective region results in irregular tangent angle variations. Then, the wavelet transform decomposes the 1-D tangent angles and captures the irregular angle variations by indicating larger magnitude of wavelet coefficients on finer scale. Finally, the upper limit for the wavelet coefficients of BGA substrate conduct paths can be established by Quality Control (QC) skills. A boundary defect can be easily located by if its wavelet coefficients exceed upper limit. Real BGA substrates with various boundary defects are used as test samples to evaluate the performance of the proposed method. Experimental results show that the proposed method achieves 100% correct identification for BGA substrate boundary defects by appropriate wavelet basis and decomposition level. The proposed method is invariant with respect to the orientation of the BGA substrates, and it does not require pre-stored templates for matching. This method is suitable for various types of BGA substrates in small batch production because precise positioning of BGA substrates and the prestored templates are not required.

Keywords: BGA substrate conduct path; Defect detection; Covariance matrix eigenvector; wavelet transform; Rotation-invariant

1. Introduction

In recent years, Printed Circuit Board (PCB) contains more conduct paths to provide functional variety but in a much smaller layout area [1]. One advanced type of PCB called the Ball Grid Array (BGA) substrate (see Fig. 1), has been extensively used to connect the solder ball array on Integrated Circuits (ICs) for electrical conductivity in Surface Mount Technology (SMT) [2]. Because the linewidths and the linespacings on BGA substrates are more sophisticated than conventional PCBs, defects are hard to detect and they could seriously disable conductivity.

Generally, the existing PCB inspection algorithms using machine vision can be classified into three categories [3]: referential approaches, non-referential approaches, and hybrid approaches. Referential approaches compare the test board image with the defect-free board stored in the image database in a pixel-by-pixel or window-by-window (i.e., a region composed by a pixel matrix) scheme to detect the defective areas. They are time-consuming for matching operations, sensitive to noise, and require large amounts of data storage for template images [4-6, 12-14]. Nonreferential approaches use design specification knowledge to verify small or medium size defects. They perform successfully only for certain types of defects (such as line widths, spacing violations, etc.). However, a serious defect such as the circuit short could be falsely treated as the conduct path. Nonreferential approaches are also error prone when rotational error is incurred [6-9]. Hybrid methods combine referential approaches and nonreferential approaches to acquire all the benefits for detecting various defect types in different sizes. Since both approaches can complement each other, hybrid methods generally achieve better identification results among the existing inspection systems. However, greater computation efforts are expected with hybrid methods. Hybrid methods also inherently suffer from rotational error and noise effects [10-11, 13].

In the past decade, wavelet transforms [15-17] became popular for localized frequency analysis because it has the capability to decompose the input signal into coarse-to-fine scales. That is, lower frequency oscillations are captured by coarse scale for global analysis and higher frequency oscillations are captured by fine scale for local analysis [18-20]. Therefore, the input signal with non-smooth or jump features over a short interval of time (e.g. local deviation) imply the occurrences of abnormality and they are readily responded by larger magnitude of wavelet coefficients on the fine scales of wavelet decomposition. For instance, wavelet function is practically feasible to detect the boundary corners of an object by using the wavelet coefficient information [21-23].

In geometrical aspect, the boundary of BGA substrate conduct paths can be considered as the combination of lines, arcs, and joints. The tangent values of boundary points are constant on the lines, change smoothly on the arcs, and vary rapidly on the joints. Thus, the 2-D boundaries of BGA substrate conduct paths are initially transformed to a 1-D θ-$\boldsymbol{s}$ representation where θ is the tangent angle as a function of arc length $\boldsymbol{s}$ along the boundaries. More specifically, the tangent angle of a boundary point is based on the eigenvector from the covariance matrix of the neighboring boundary points over a small region of support [24]. Further, since a joint and a boundary defect can be respectively treated as single corner and multiple jag corners (see Fig. 2), irregular tangent variations are expected for boundary corner(s). Therefore, the 1-D θ-$\boldsymbol{s}$ representation for the boundary of BGA substrate conduct paths is then decomposed by wavelets to detect these local anomalies by using wavelet coefficient information.

In this study, four serious and common boundary defect types including open, short, mousebite, and spur (see Fig. 2(b)-(e)) on BGA substrate conduct paths are detected by the proposed wavelet-based approach. However, these four defect types are not classified in this work. The proposed BGA substrate inspection algorithm does not require prestored templates for matching process. Besides, this wavelet-based detection for boundary defects is invariant to rotation so it is able to reduce the sensitivity of angular error with respect to traditional PCB inspection methods. Therefore, this approach is particularly suitable for various BGA substrate types in small batch production because

(a)

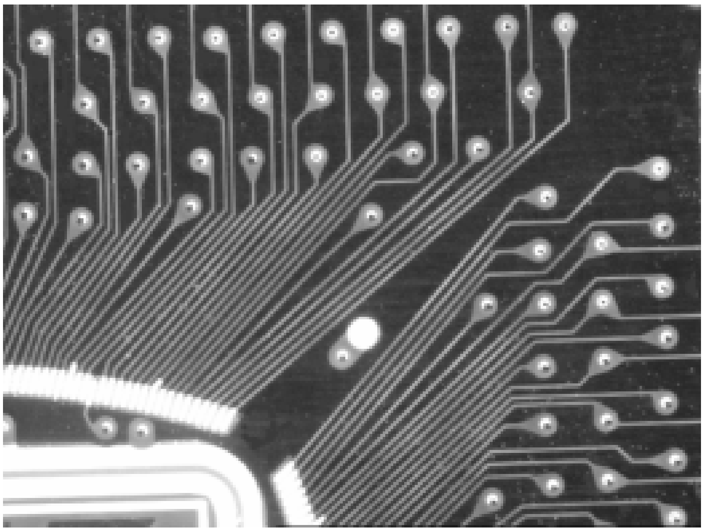

(b)

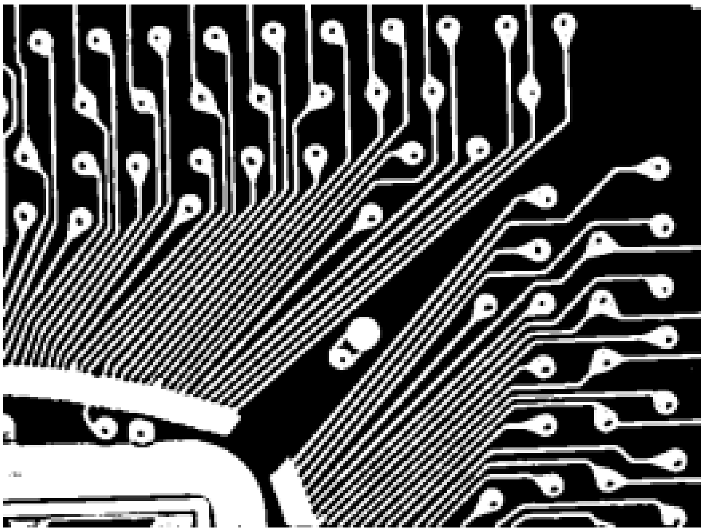

Fig. 1. Real BGA substrate conduct paths (right-upper side). (a) Original image with a 25mm x 18mm field of view and 640 x 480 pixels resolution. (b) Binary image of the BGA substrate shown in (a).

(a) (b) (c) (d) (e)

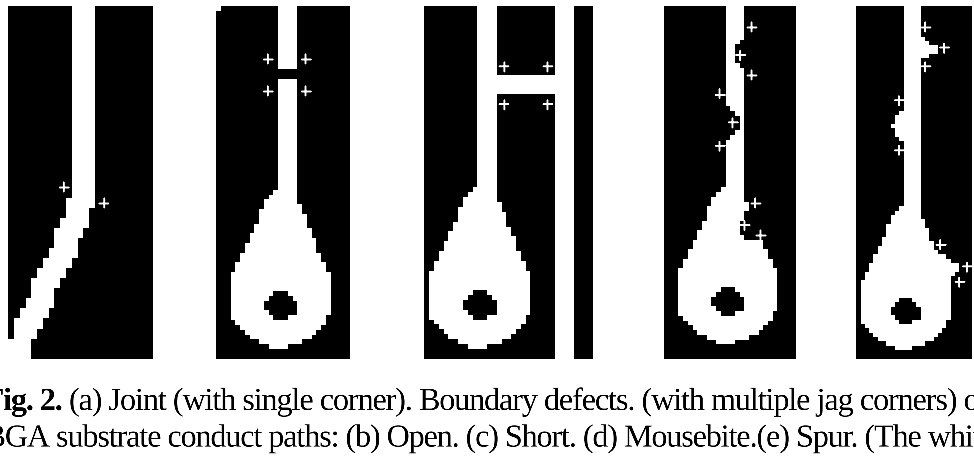

Fig. 2. (a) Joint (with single corner). Boundary defects. (with multiple jag corners) on BGA substrate conduct paths: (b) Open. (c) Short. (d) Mousebite.(e) Spur. (The white cross “+” represents a detected corner.)

it requires no precise alignment for the BGA substrates under inspection. Moreover, since one circular pad connects one conduct path on BGA substrate, the junction shape of conduct paths can be ignored to deal with in this research.

This paper is organized as follows: In section 2, the eigenvector of the covariance matrix from a boundary segment for calculating the tangent angle of each boundary point is presented. Furthermore, wavelet transform is also briefly discussed in this section. The proposed algorithm based on the tangent representation and the wavelet decomposition approximation in multiresolution to localize the BGA substrate conduct path boundary defects is described and illustrated in section 3. Then, experimental verification of the proposed method in various orthogonal wavelets is shown in section 4. Finally, the conclusion is given in section 5.

2. Covariance Matrices Enginvector and Wavelet Decomposition

2.1 Tangent representation by covariance matrices enginvector

The binary image of a BGA substrate is pre-processed by boundary following [24] to extract the X-Y coordinates of each boundary point along the conduct paths. Let n sequential digital points describe a boundary $\boldsymbol{P}$,

$$\boldsymbol{P} = \{p_i = (x_i, y_i),\ i = 1, 2, 3, \ldots, n\}$$

where p_{i+1} is adjacent to p_i on $\boldsymbol{P}$. Further, let $\boldsymbol{N_s}(p_i)$ denote a small boundary segment centering on point p_i over the region of support between points p_{i-s} and p_{i+s} for some integer $\boldsymbol{s}$, i.e.,

$$\boldsymbol{N_s}(p_i) = \{p_j \mid i-\boldsymbol{s} \leqq j \leqq i+\boldsymbol{s}\}$$

Therefore, the covariance matrix $\boldsymbol{M}$ of a boundary segment $\boldsymbol{N_s}(p_i)$ is given by

$$\boldsymbol{M} = \begin{bmatrix} \boldsymbol{m}_{11} & \boldsymbol{m}_{12} \\ \boldsymbol{m}_{21} & \boldsymbol{m}_{22} \end{bmatrix}$$

where

$$\boldsymbol{m}_{11} = [\frac{1}{2s+1}\sum_{j=i-s}^{i+s} x_j^{\,2}] - \bar{x}_i^{\,2}$$

$$\boldsymbol{m}_{22} = [\frac{1}{2s+1}\sum_{j=i-s}^{i+s} y_j^{\,2}] - \bar{y}_i^{\,2}$$

$$\boldsymbol{m}_{12} = \boldsymbol{m}_{21} = [\frac{1}{2s+1}\sum_{j=i-s}^{i+s} x_j y_j] - \bar{x}_i \bar{y}_i$$

$$\bar{x}_i = \frac{1}{2\boldsymbol{s}+1}\sum_{j=\boldsymbol{i}-\boldsymbol{s}}^{\boldsymbol{i}+\boldsymbol{s}} x_j$$

$$\bar{y}_i = \frac{1}{2\boldsymbol{s}+1}\sum_{j=\boldsymbol{i}-\boldsymbol{s}}^{\boldsymbol{i}+\boldsymbol{s}} y_j$$

$\bar{x}_i$ and $\bar{y}_i$ are the geometrical center of $\boldsymbol{N_s}(p_i)$. The covariance matrix $\boldsymbol{M}$ is a 2 x 2, symmetric, and positive semidefinite matrix. The eigenvalues λ_1 λ_2 and the eigenvectors $\boldsymbol{E}_1$ and $\boldsymbol{E}_2$ of the matrix $\boldsymbol{M}$ are obtained from following equations [25]:

$$\boldsymbol{E}_1 = \begin{bmatrix} \boldsymbol{e}_{1x} \\ \boldsymbol{e}_{1y} \end{bmatrix} = \begin{bmatrix} \dfrac{\boldsymbol{m}_{12}}{\sqrt{(\lambda_1 - \boldsymbol{m}_{11})^2 + \boldsymbol{m}_{12}{}^2}} \\ \dfrac{(\lambda_1 - \boldsymbol{m}_{11})}{\sqrt{(\lambda_1 - \boldsymbol{m}_{11})^2 + \boldsymbol{m}_{12}{}^2}} \end{bmatrix}$$

$$\boldsymbol{E}_2 = \begin{bmatrix} \boldsymbol{e}_{2x} \\ \boldsymbol{e}_{2y} \end{bmatrix} = \begin{bmatrix} \dfrac{\boldsymbol{m}_{12}}{\sqrt{(\lambda_2 - \boldsymbol{m}_{11})^2 + \boldsymbol{m}_{12}{}^2}} \\ \dfrac{(\lambda_2 - \boldsymbol{m}_{11})}{\sqrt{(\lambda_2 - \boldsymbol{m}_{11})^2 + \boldsymbol{m}_{12}{}^2}} \end{bmatrix}$$

$$\lambda_1 = (\boldsymbol{m}_{11} + \boldsymbol{m}_{22} + \sqrt{(\boldsymbol{m}_{11} - \boldsymbol{m}_{22})^2 + 4\boldsymbol{m}_{12}{}^2}\ )$$

$$\lambda_2 = (\boldsymbol{m}_{11} + \boldsymbol{m}_{22} - \sqrt{(\boldsymbol{m}_{11} - \boldsymbol{m}_{22})^2 + 4\boldsymbol{m}_{12}{}^2}\ )$$

Where λ_1 and λ_2 are the eigenvalues corresponding to $\boldsymbol{E}_1$ and $\boldsymbol{E}_2$. The eigenvectors $\boldsymbol{E}_1$ and $\boldsymbol{E}_2$ represent respectively the tangent (major axis) and the normal (minor axis) directions for point p_i over the segment $\boldsymbol{N}_s(p_i)$. Therefore, the tangent angle for point p_i is simply defined as following:

$$\boldsymbol{tan}\theta(p_i) = \frac{\boldsymbol{e}_{1y}}{\boldsymbol{e}_{1x}} = \frac{(\lambda_1 - \boldsymbol{m}_{11})}{\boldsymbol{m}_{12}}$$

$$\theta(p_i) = \tan^{-1}\left(\frac{\lambda_1 - \boldsymbol{m}_{11}}{\boldsymbol{m}_{12}}\right)$$

In general, the magnitude of $\theta(p_i)$ is between –90° and 90°. However, in order to avoid the occurrence of “jump” for two adjacent boundary points due to quantization noise, $\theta(p_i)$ is defined to be between 0 and 90° in this study. Fig. 3(a) shows a portion of BGA substrate conduct paths with synthetic defects, there are 1470 boundary points on the conduct paths. Number 1 denotes the starting boundary point and white arrow indicates the boundary following direction. The defective regions labeled by capital characters A-H in Fig. 3(a) are extracted and the corresponding 1-D θ-s curve diagrams are respectively illustrated in Fig. 3(b). Because the boundary defects are composed by multiple corners, the 1-D θ-s curve of defects in Fig. 3(b) are either singular (e.g. region A-D) or high frequency oscillations in a short interval of boundary segment (e.g. region E-H). Moreover, a small portion of defective BGA substrate conduct path in 15° and 30° orientations and the corresponding 1-D θ-s curves are respectively show in Fig. 4(a) and Fig. 4(b) to demonstrate the rotational effect. Singularity and high frequency oscillations in 1-D θ-s remain for defective regions even they are in different orientations.

(a)

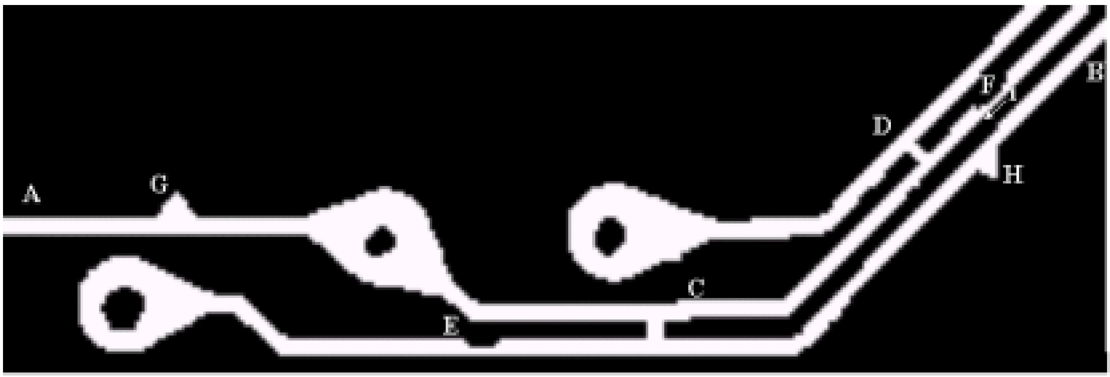

(b)

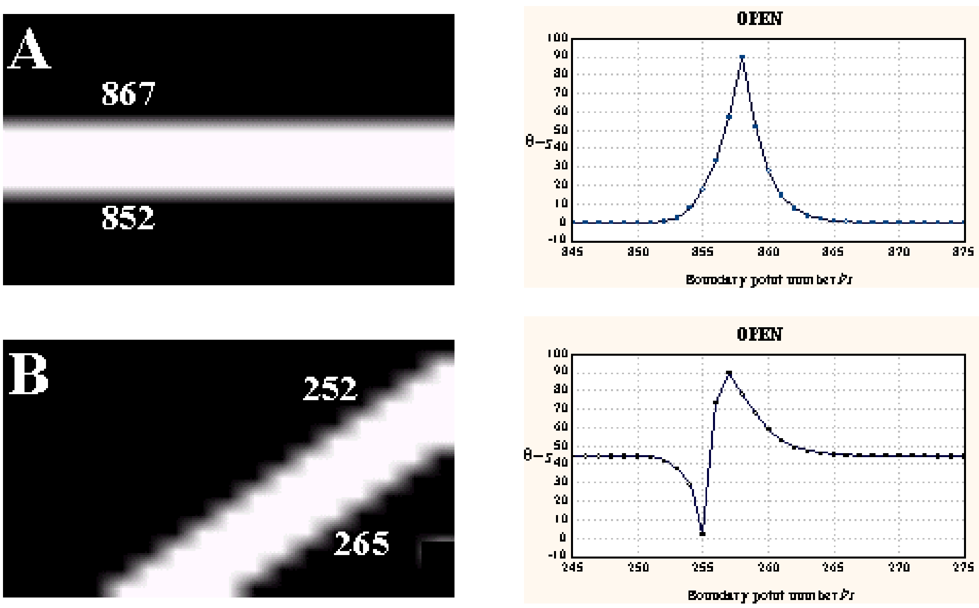

Fig. 3. (a) A portion of BGA substrate conduct paths with synthetic defects, defective regions are respectively labeled by capital characters A-H. (b) Left side- open defects (A, B), short defects (C, D), mousebite defects (E, F), and spur defects (G, H). Right side- the corresponding 1-D ***θ-s*** curve diagrams.

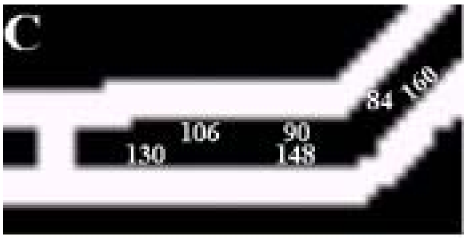
C
106
90
130
148
84
160

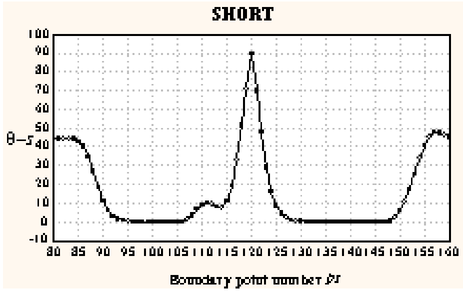
SHORT
Boundary point number ps

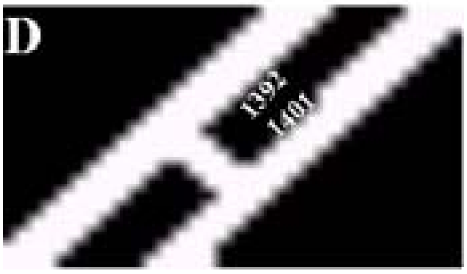
D
1392
1401

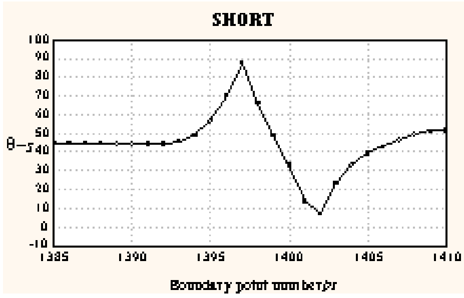
SHORT
Boundary point number ps

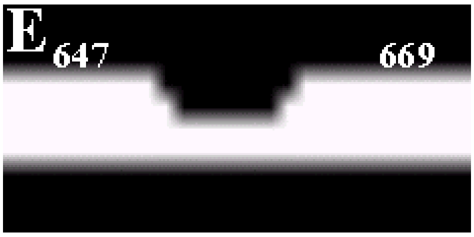
E
647
669

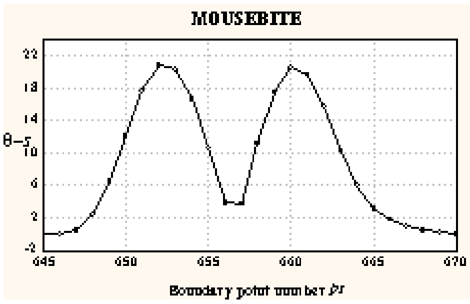
MOUSEBITE
Boundary point number ps

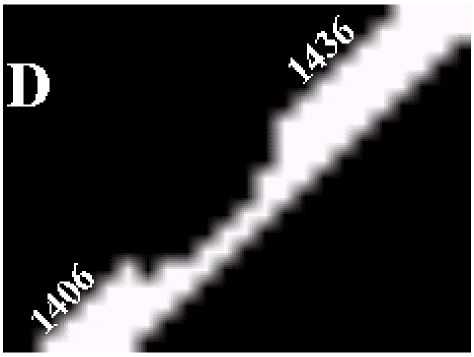
D
1436
1406

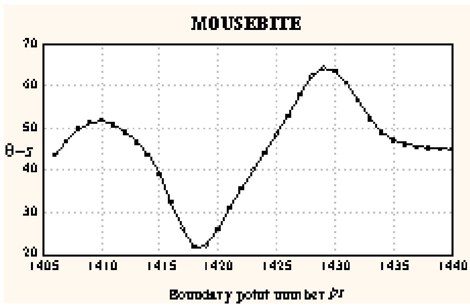
MOUSEBITE
Boundary point number ps

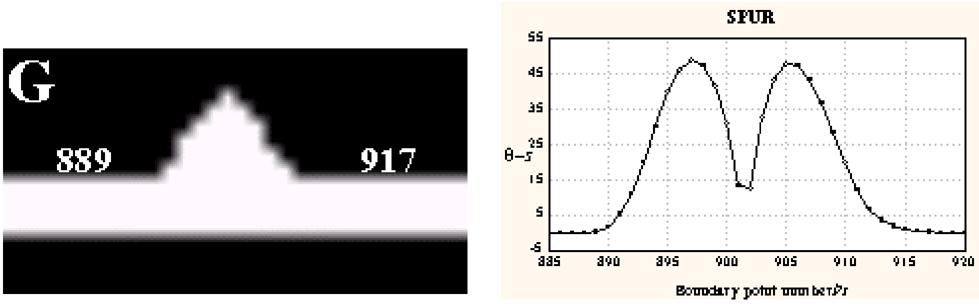
G
889
917
SPUR
θ−s
Boundary point number Pi

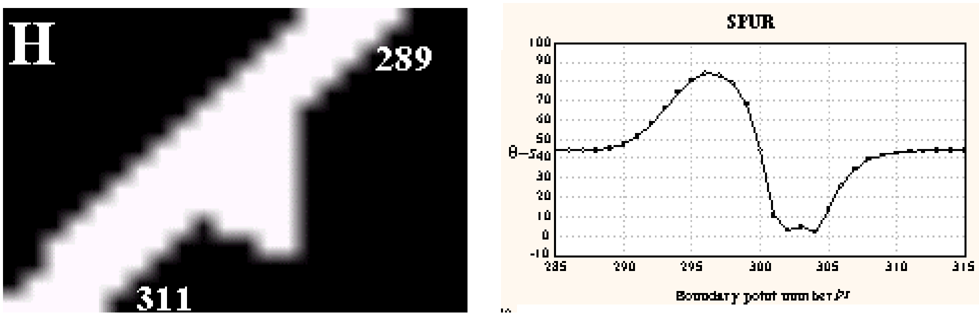
H
289
311
SPUR
θ−s
Boundary point number Pi

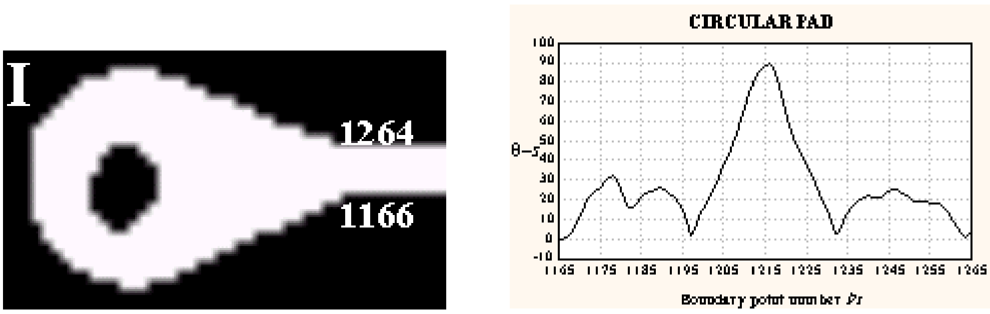
I
1264
1166
CIRCULAR PAD
θ−s
Boundary point number Pi

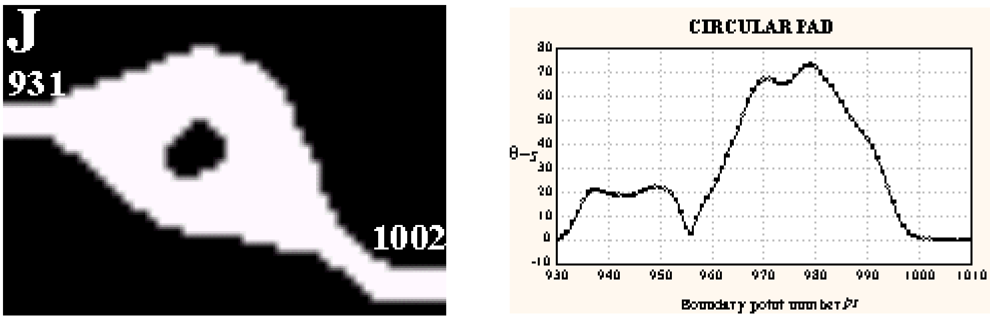
J
931
1002
CIRCULAR PAD
θ−s
Boundary point number Pi

(a) (b)

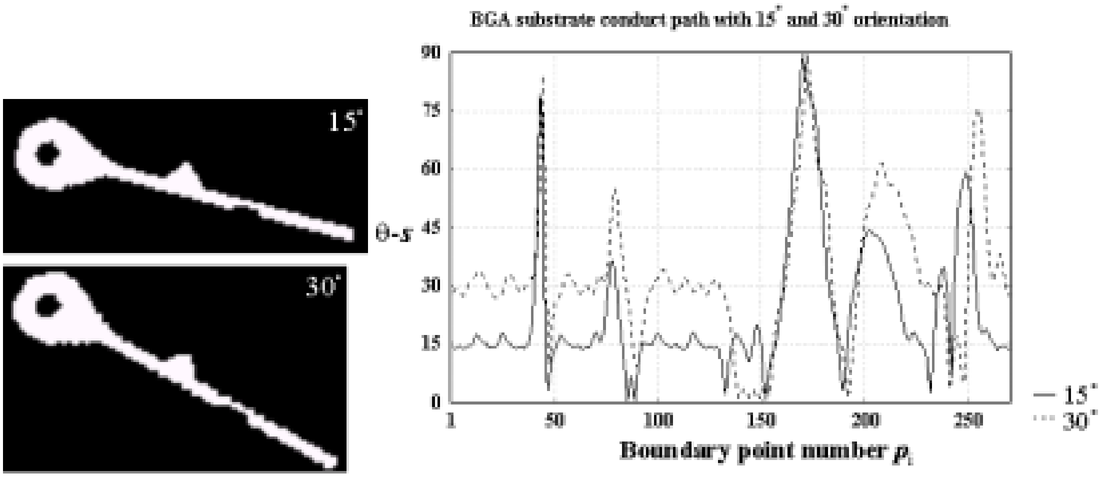

Fig. 4. (a) A small portion of defective BGA substrate conduct path in 15° and 30° orientations. (b) The corresponding 1-D θ-s curves for (a).

2.2 Wavelet decomposition

With the similar principle in Fourier transform, we can use a linear combination of wavelet function to represent a signal $f(t)$. Wavelets are generated by orthogonal father wavelets ϕ and mother wavelets ψ. Father wavelets represent the smooth and low-frequency parts of a signal and mother wavelets represent the detail and high-frequency parts of a signal. There are various wavelet bases such as *Harr, Daublets, Symmlets,* and *Coiiflets* [15, 17]. They are different in continuity and symmetry. The *Harr* wavelet is discontinuous and it has compact support length. The wavelet basis "d4" represents *Daublets* with support length 4. The wavelet basis "s12" (*Symmlets* with support length 12) is wider and smoother than the "s4" wavelet basis. The number is related to the width and smoothness of the wavelet function [20].

For a continuous signal $\boldsymbol{f}(\boldsymbol{t})$, it can be approximated by the orthogonal wavelet series. The approximation is called multiresolution decomposition (MRD) and expressed as follows [20]:

$$\boldsymbol{f}(\boldsymbol{t}) \approx \boldsymbol{S}_J(\boldsymbol{t})+\boldsymbol{D}_J(\boldsymbol{t}) +\boldsymbol{D}_{J-1}(\boldsymbol{t})+\ldots\boldsymbol{D}_2(\boldsymbol{t})+\boldsymbol{D}_1(\boldsymbol{t})$$

where

$$\boldsymbol{S}_J(\boldsymbol{t})=\sum_k s_{J,k}\phi_{J,k}(\boldsymbol{t}),\ \boldsymbol{D}_j(\boldsymbol{t}) = \sum_k d_{j,k}\psi_{j,k}(\boldsymbol{t})$$

$$\phi_{J,k}(\boldsymbol{t}) = 2^{-J/2}\phi\left(\frac{\boldsymbol{t}-2^J k}{2^J}\right),\quad \psi_{j,k}(\boldsymbol{t}) = 2^{-j/2}\psi\left(\frac{\boldsymbol{t}-2^j k}{2^J}\right)$$

$\boldsymbol{S}_J(\boldsymbol{t})$: the smooth part of the signal on the Jth scale

$\boldsymbol{D}_j(\boldsymbol{t})$: the detail part of the signal on the jth scale

J : the number of multiresolution scales

k : translated parameter, $k \in [1, \frac{n}{2^j}]$, k is integer.

n : the number of points to form the signal on $\boldsymbol{t}$ domain

j : scaled parameter (j = 1, 2, …, J)

$s_{J,k}$: the wavelet coefficients for the smooth part of the signal on the Jth scale

$d_{j,k}$: the wavelet coefficients for the detail part of the signal on the jth scale

$s_{J,k} \approx \int \phi_{J,k}(\boldsymbol{t})\ \boldsymbol{f}(\boldsymbol{t})d\boldsymbol{t}$, $d_{j,k} \approx \int \psi_{j,k}(\boldsymbol{t})\ \boldsymbol{f}(\boldsymbol{t})d\boldsymbol{t}$, $s_{J,k}$, $d_{j,k} \in$ R

In practice, the coarse scale components $\boldsymbol{S}_\mathrm{J}$ and $\boldsymbol{D}_\mathrm{J}$ mainly describe the lower frequency oscillations of $\boldsymbol{f}(\boldsymbol{t})$ on wider $\boldsymbol{t}$ domain. Conversely, higher frequency oscillations of $\boldsymbol{f}(\boldsymbol{t})$ on narrower $\boldsymbol{t}$ domain are mainly captured by fine scale detail $\boldsymbol{D}_2$ and $\boldsymbol{D}_1$ components. On fine scale, the wavelet coefficients corresponding to high fluctuations are much greater than the wavelet coefficients on the smooth part of the signal in magnitude. For instance, the 1-D $\boldsymbol{\theta}$-$\boldsymbol{s}$ curve from Fig. 3(a) is used as a input signal $\boldsymbol{f}(p_i)$. The MRD for $\boldsymbol{f}(p_i)$ by *Coiiflets* with support length 6 (e.g. c6 wavelet basis) and 3 decomposition levels (e.g. J = 3) is demonstrated in Fig. 5. In Fig. 5, the coarse representation of $\boldsymbol{f}(p_i)$ is globally captured by $\boldsymbol{S}_3$ and $\boldsymbol{D}_3$ scales, the singular and high fluctuation parts of $\boldsymbol{f}(p_i)$ are locally reflected by larger magnitude of wavelet coefficients on $\boldsymbol{D}_2$ and $\boldsymbol{D}_1$ scales. In addition, if more decomposition levels are employed (e.g. J = 5), the smooth parts of signal are roughly captured by $\boldsymbol{S}_5$ and $\boldsymbol{D}_5$ scales. Middle fluctuation parts of signal are captured by $\boldsymbol{D}_3$, and $\boldsymbol{D}_4$ scales. High frequency oscillations are mainly captured by $\boldsymbol{D}_2$ and $\boldsymbol{D}_1$ scales. The impact of different decomposition level number is shown in Fig. 6. However, the wavelet coefficients on $\boldsymbol{D}_2$ and $\boldsymbol{D}_1$ scales are identical regardless of the decomposition level number. Moreover, owing to the inherent "end effect" of wavelet transform, larger magnitude of wavelet coefficients on both ends for each decomposition level are inevitable. The end effect should be ignored in further analysis.

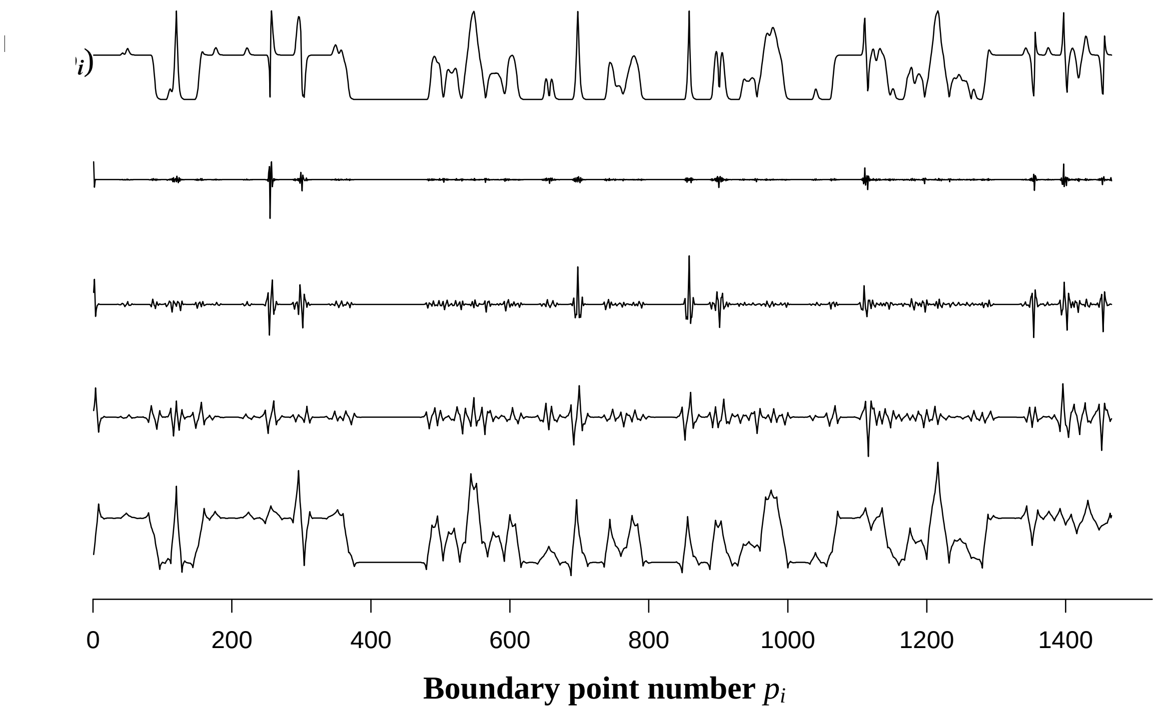

Fig. 5. The MRD for the 1-D ***θ-s*** curve from Fig. 3(a) (***f***(p_i)) by wavelet basis c6 and 3 decomposition levels.

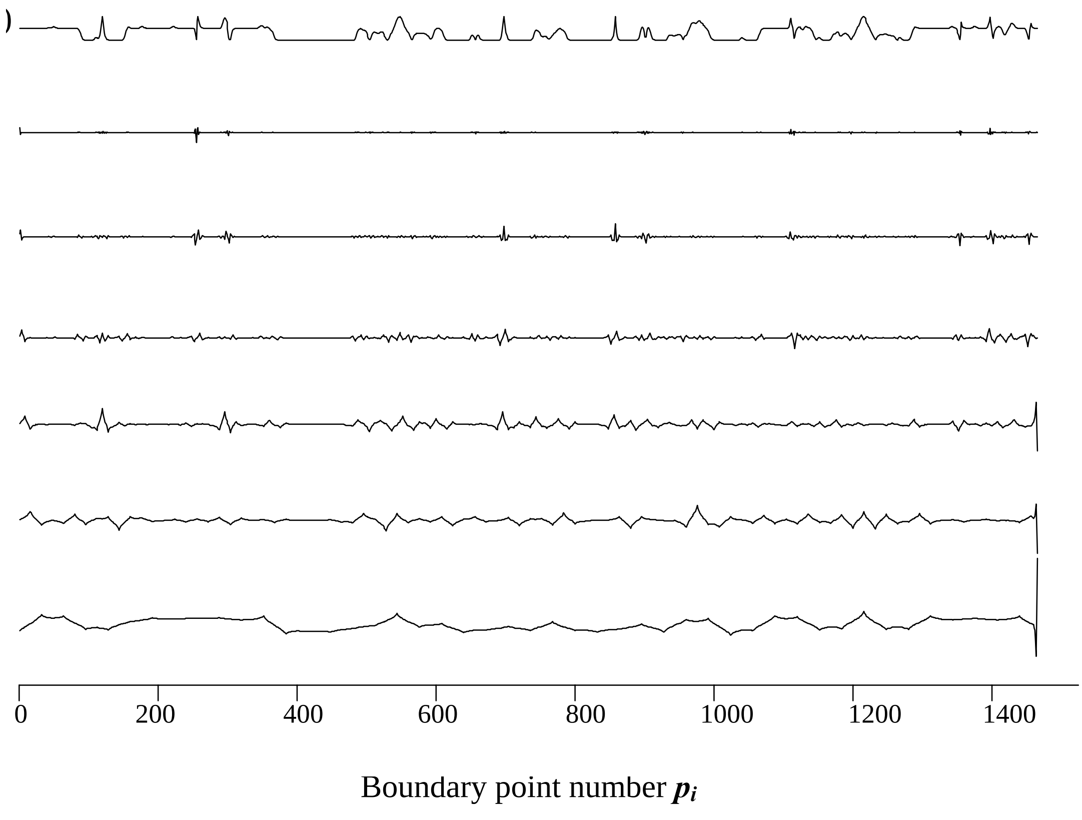

Fig. 6. The MRD for the 1-D ***θ-s*** curve from Fig. 3(a) (***f***(p_i)) by wavelet basis c6 and 5 decomposition levels.

3. The proposed approach for detecting the boundary defects

Since the defective regions such as open, short, mousebite, and spur on BGA substrate conduct paths boundary are composed by multiple jag corners, they provides irregular fluctuation behavior and singularity on 1-D ***θ-s*** curve. However, the circular pad on BGA substrate conduct paths may also show multiple jag corners (see Fig. 7). A circular pad may be misclassified as a defect. Therefore, we could localize a boundary defect candidate (i.e. including true defects or circular pads) if a boundary point p_i has extremely large wavelet coefficients on $\boldsymbol{D}_2$ or $\boldsymbol{D}_1$ scales in MRD. The wavelet coefficients on $\boldsymbol{D}_2$ and $\boldsymbol{D}_1$ of a boundary point p_i are denoted by **WCD1**(p_i) and **WCD2**(p_i), respectively. Then, the overall wavelet coefficients for the boundary points on a potential defective region and the correlation coefficient matching with circular pad are measured to eliminate the circular pads among the defect candidates. In this manner, the true defects can be located.

(a) (b) (c)

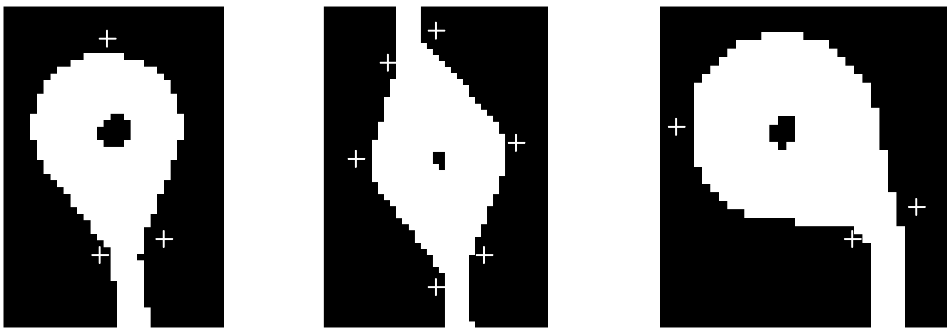

Fig. 7. (a)(b)(c) Circular pads composed by multiple jag corners (The white cross "+" represents a detected corner.). (d) Left side- circular pads are extracted from Fig. 3(a). Right side- the corresponding 1-D ***θ-s*** curve diagrams.

(d)

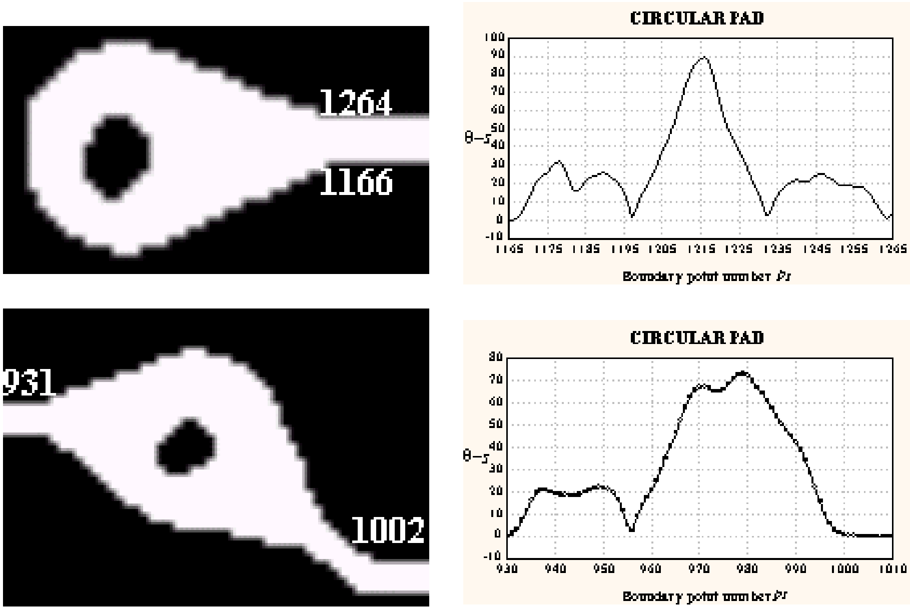

(**Fig. 7.** Continued)

3.1 Locating the defects candidates

To distinguish the potential defects and non-defective regions on BGA substrate conduct paths, a defect-free BGA substrate is used to collect the normal wavelet coefficients from joints, lines, and digital quantization effect by MRD. The wavelet coefficients of circular pads are excluded because they are potential defects. In addition, since the wavelet transform has better locating ability and less noise effect at the finest scale [21, 22], so the wavelet coefficients on $\boldsymbol{D}_1$ scale are collected. The amount of observation is greater than 10000 to estimate the population mean (μ_{WCD1}) and standard deviation (σ_{WCD1}) for the regular wavelet coefficients on $\boldsymbol{D}_1$ scale. Traditionally, a flaw occurs when its specification is out of the control limits $\mu \pm 3\sigma$ by quality control skill. As mentioned, the wavelet coefficient of a defective region point is much larger in magnitude with respect to the wavelet coefficient of a non-defective region point on $\boldsymbol{D}_2$ and $\boldsymbol{D}_1$ scales. In order to avoid false-alarm error, a boundary point p_i is defined as one of potential defective region points (denoted by p_m) if **WCD1**(p_m) is out of $\mu_{\mathrm{WCD1}} \pm 6\sigma_{\mathrm{WCD1}}$. By doing so, 99.999% of the non-defective regions are eliminated and the defect candidates are surely located.

3.2 Identifying true defects among defect candidates

From section 3.1, the potential defects are located by the wavelet coefficients on $\boldsymbol{D}_1$ scale and simple quality control technique. In this section, the defective candidates will be classified into real defects and circular pads by measuring their energy value and correlation coefficient matching with circular pad. The alias "energy" represents the magnitude of the wavelet coefficients in absolute value for a segment of signal $\boldsymbol{f}(\boldsymbol{t})$. The potential defective region points for a specified defect can be identified by expanding from p_m in forward and back directions of boundary following. Two adjacent points are incorporated into the same region if the tangent angle difference in absolute value between them is greater than 1°. The procedure is iterated until the above constraint is violated. That is,

potential defective region points = $\{p_i \mid i = s, s+1, \ldots, m-1, m, m+1, \ldots, t-1, t\}$

where

$|\theta(p_i) - \theta(p_{i+1})| \geq 1°$ and $|\theta(p_i) - \theta(p_{i-1})| \geq 1° \quad \forall\ i$

$|\theta(p_s) - \theta(p_{s-1})| < 1°$ and $|\theta(p_t) - \theta(p_{t+1})| < 1°$

The boundary points p_s and p_t are the start point and terminate point for this potential defective region, respectively. Thus, the region of a potential defect can be identified. The average energy for a defect candidate is abbreviated as μ_{EDC} and determined as follows:

$$\mu_{\mathrm{EDC}} = \frac{\sum_{i=s}^{t} |\,\mathbf{WCD1}(p_i)\,|}{t - s + 1}$$

A defect candidate will be considered as a non-defective region if its μ_{EDC} is less than $\mu_{\mathrm{WCD1}} + 3\sigma_{\mathrm{WCD1}}$ by quality control practice. Most of smooth circular pads as shown in Fig. 7(a) and 7(b) are no longer potential defects during this stage because their μ_{EDC} are not able to exceed $\mu_{\mathrm{WCD1}} + 3\sigma_{\mathrm{WCD1}}$ However, circular pads with sharp corner(s) (see Fig. 7(c)) remain defect candidates. The 1-D ***θ-s*** curve for the boundary points of circular pad with salient corner(s) shown in Fig. 7(c) is treated as "golden data set" to measure the similarity with the 1-D ***θ-s*** curve of the rest of potential defective regions. There are M boundary points in golden data set, the start point and terminate point are respectively denoted by p_{gs} and p_{ts}. The rest of defect candidate is recognized as a circular pad if the correlation coefficient between its 1-D ***θ-s*** curve and the golden data set is greater than 0.9. The correlation coefficient (ρ) is defined as follows:

$$\rho = \frac{\sum_{j,k=1}^{\mathrm{n}} \theta(p_j)\theta(p_k) - \mathrm{n}\,\mu_j\mu_k}{\mathrm{n}\,\sigma_j\sigma_k}$$

where

$\theta(p_j)$: the tangent angle extracted from golden data set (j = 1,2, …, n)

μ_j and σ_j : mean and standard deviation of $\theta(p_j)$ (j = 1,2, …, n)

$\theta(p_k)$: the tangent angle extracted from the rest of potential defective region (k = 1, 2, …, n)

μ_k and σ_k : mean and standard deviation of $\theta(p_k)$ (k = 1, 2, …, n)

n = Min.{M, N}

N: the number of boundary points in the rest of potential defective region

If M ≥ N, $p_j = p_{gs}$ (j = 1), $p_j = p_{gt}$ (j = n), $p_j = p_{\mathrm{int}(\frac{\mathrm{M}}{\mathrm{N}} \times j)}$ (j = 2, 3, …, n-2 , n-1)

If N > M, $p_k = p_{ds}$ (k = 1), $p_k = p_{dt}$ (k = n), $p_k = p_{\mathrm{int}(\frac{\mathrm{N}}{\mathrm{M}} \times k)}$ (k = 2, 3, …, n-2, n-1)

p_{gs} and p_{ts} : the start point and terminate point for the rest of defects candidates

Since all the circular pads in various shapes are distinguished, the rest of defect candidates are identified as true defects. In short, a defect candidate is identified as a true defect only if its μ_{EDC} exceeds $\mu_{\mathrm{WCD1}} + 3\sigma_{\mathrm{WCD1}}$ and its correlation coefficient (ρ) with golden data set is less than 0.9. The defects detecting procedure is summarized in Fig. 8.

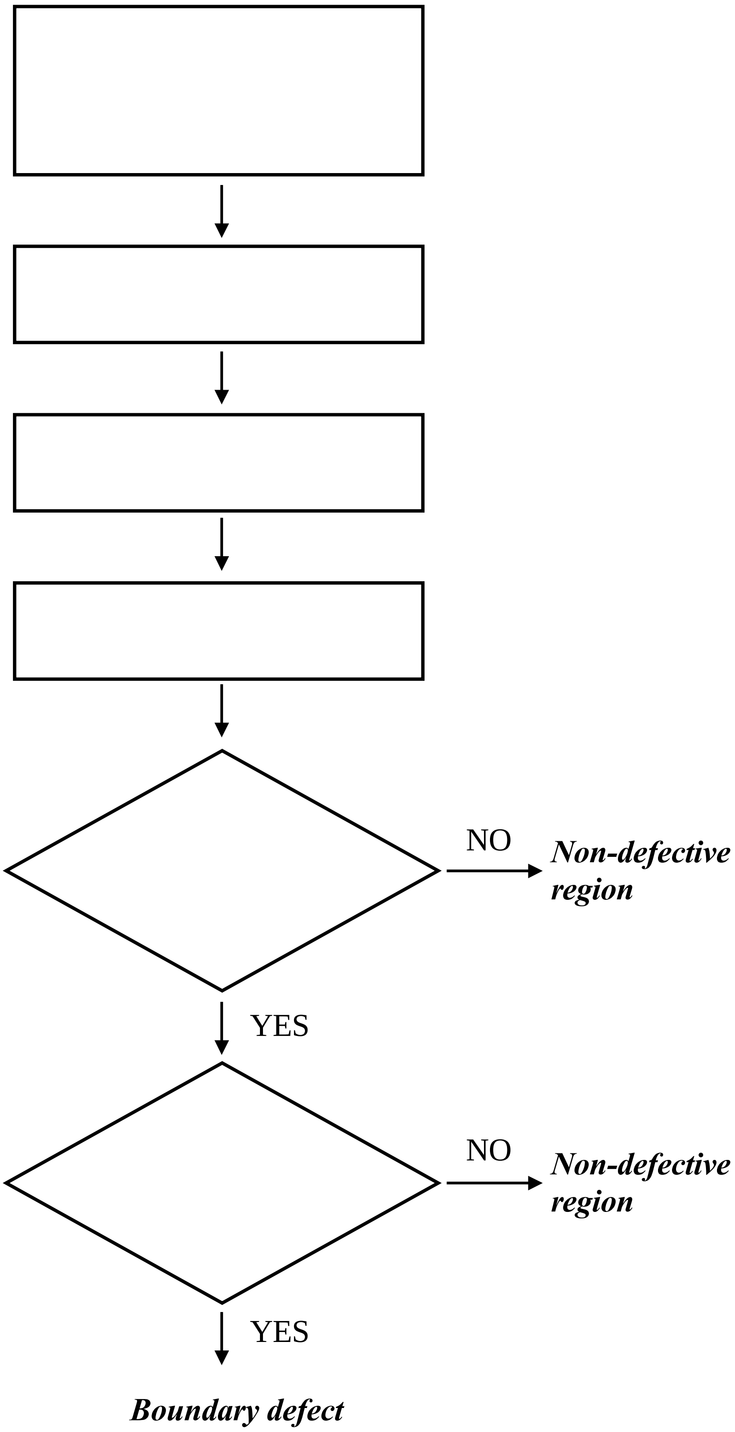

Fig. 8. The summarized defect-detecting procedure

4. Experimental Results

Two experiments are conducted in this study. One evaluates the performance of the proposed defect detection method and the other one verifies its rotation-invariant property. A LED ring lighting source and a 25mm lens with 12mm extension ring are used to increase the visibility of the BGA substrate conduct path. The defect detection program is edited in the C language and executed on the vision package software named “Optimas” using a personal computer.

In the first experiment, the bottom side of a real BGA substrate (shown in Fig. 9) is captured as the test image sample to evaluate the defect detection capabilities of the proposed algorithms. The test sample is captured in a 25mm x 20mm field of view, which corresponds to 640 x 480 pixels in the image. There are 40 synthetic boundary defects in the test sample, which includ 10 opens, 10 shorts, 10 mousebites, and 10 spurs. Both simple and complicated shape defects are included to fit the real inspection environment. The detection errors come from two sources: 1) False acceptance (i.e., a normal region is detected as a defect), 2) False rejection (i.e., failure to alarm a true defect). Moreover, various wavelet bases such as Haar, s4, s6, s8, d4, d6, d8, c6, and c12 [20] must be incorporated to realize the effect on this experiment. The population mean (μ_{WCD1}) and standard deviation (σ_{WCD1}) for each wavelet basis aforementioned is calculated in advance. The region of support for covariance matrix eigenvector is 7 (i.e., $\boldsymbol{s}$ value = 3) to reveal the local property of a corner. The experimental result is summarized in Table 1. In Table 1, detection errors occur from the wavelet bases s6, s8, d6, d8, and c12 because the longer support length may over smooth the input signal. Shorter support length wavelet basis such as Haar is sensitive to noise, it causes significant false acceptance errors. For a total of 40 defects in the test image, the wavelet bases s4, d4, and c6 are able to reach 100% identification for boundary defects.

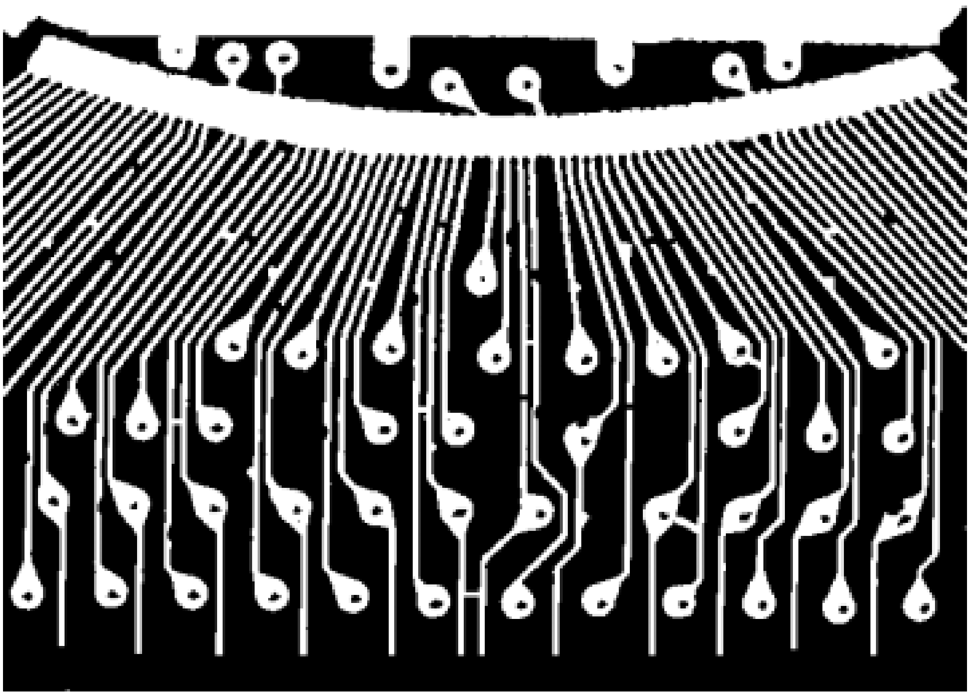

Fig. 9. BGA substrate test sample image.

Table. 1. The defect detection result for wavelets s4, s6, s8, d4, d6, d8, c6, c12, and Haar on $\boldsymbol{D}_1$ scale at $\boldsymbol{s}$ = 3.

wavelet basis	**s4**		**s6**		**s8**		**d4**		**d6**		**d8**		**c6**		**c12**		**Haar**	
μ_{WCD1}	0.000139		-0.00025		0.0002		0.000137		-0.00024		0.00008		-0.000134		-0.000124		-0.0001	
σ_{WCD1}	0.374		0.2004		0.4649		0.368		0.2002		0.3306		0.368		0.0989		0.6507	
Detection error	**I**	**II**	**I**	**II**	**I**	**II**	**I**	**II**	**I**	**II**	**I**	**II**	**I**	**II**	**I**	**II**	**I**	**II**
The number of error occurs	0	0	2	2	0	10	0	0	2	2	0	5	0	0	0	6	8	3
Total	0		4		10		0		4		5		0		6		11	

error **I** : False acceptance, error **II** : False Rejection

In the second experiment, images in varying orentation including 0°, 5°, and 15° of a BGA substrate are used to verify the rotational effect. In practice, rotational errors exceeding 15° may not exist in the real BGA substrate inspection. binary image involves 40 synthetic defects containing 10 opens, 10 shorts, 10 mousebites, and 10 spurs (see Fig. 10(a)). The images in 5° and 15° rotations with respect to the original 0° image in Fig. 10(a) are shown in Figs. 10(b)-10(c), respectively. From the result of the first experiment, only three effective wavelet bases s4, d4, and c6 are implemented in the second experiment. The required parameters μ_{WCD1} and σ_{WCD1} for wavelets s4, d4, and c6 are the same as the first experiment for a given region of support $\boldsymbol{s}$ = 3. The defect detection from the images in various orientations reach 100% identification as well.

(a) (b) (c)

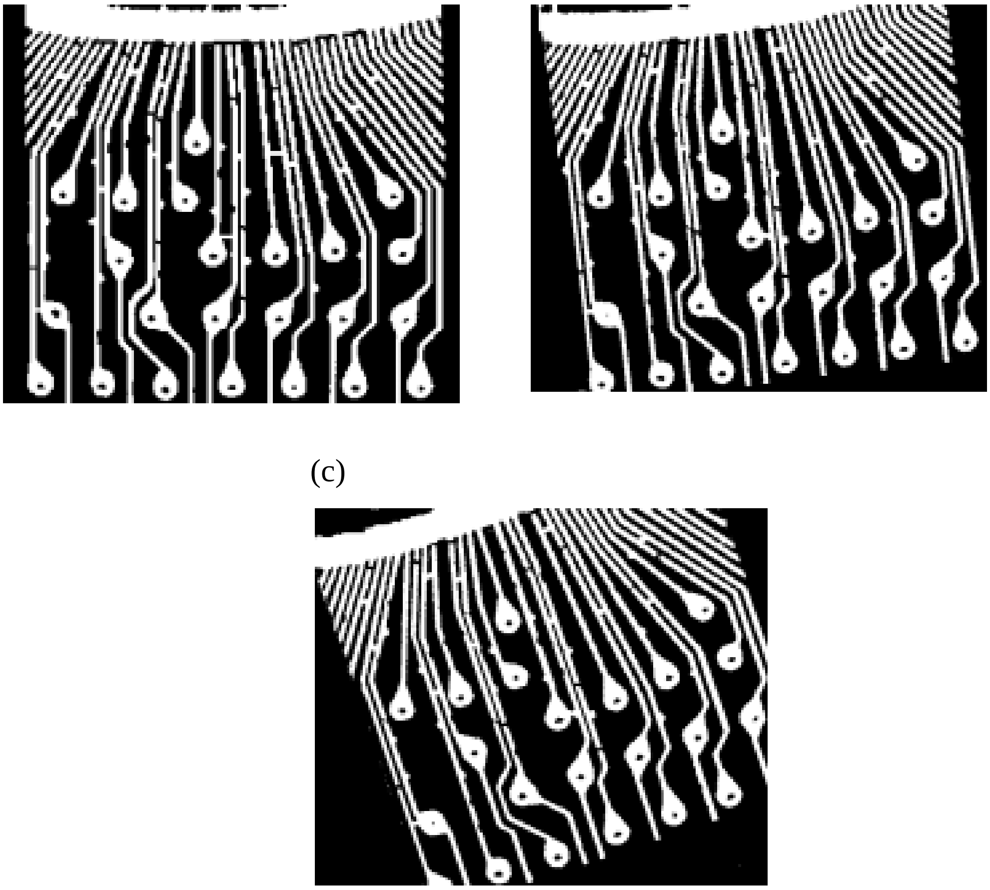

Fig. 10. Binary images of a BGA substrate in varying orientations:
(a) 0°, (b) 5°, (c) 15°.

Two real defective BGA substrates shown in Fig. 11(a) and Fig. 12(a) are used to demonstrate the proposed approach in the real inspection environment. Fig. 11(a) shows “short” and “spur” defects. Fig. 12(a) shows “open” defects. The images in 45° and 90° orientations for Fig. 11(a) are respectively illustrated in Fig. 11(c) and Fig. 11(d). The short defects and the spur defects are reliably detected, which are respectively marked by white squares and circles dotted lines in the images. Each cross sign points out the position with the largest absolute value of wavelet coefficient for each defect. With the same practice for defects in Fig. 12(a), the open defects are detected and encircled by white dotted lines in Fig. 12(c), and Fig. 12(d), respectively. The results reveal that all defects are reliably identified and well localized.

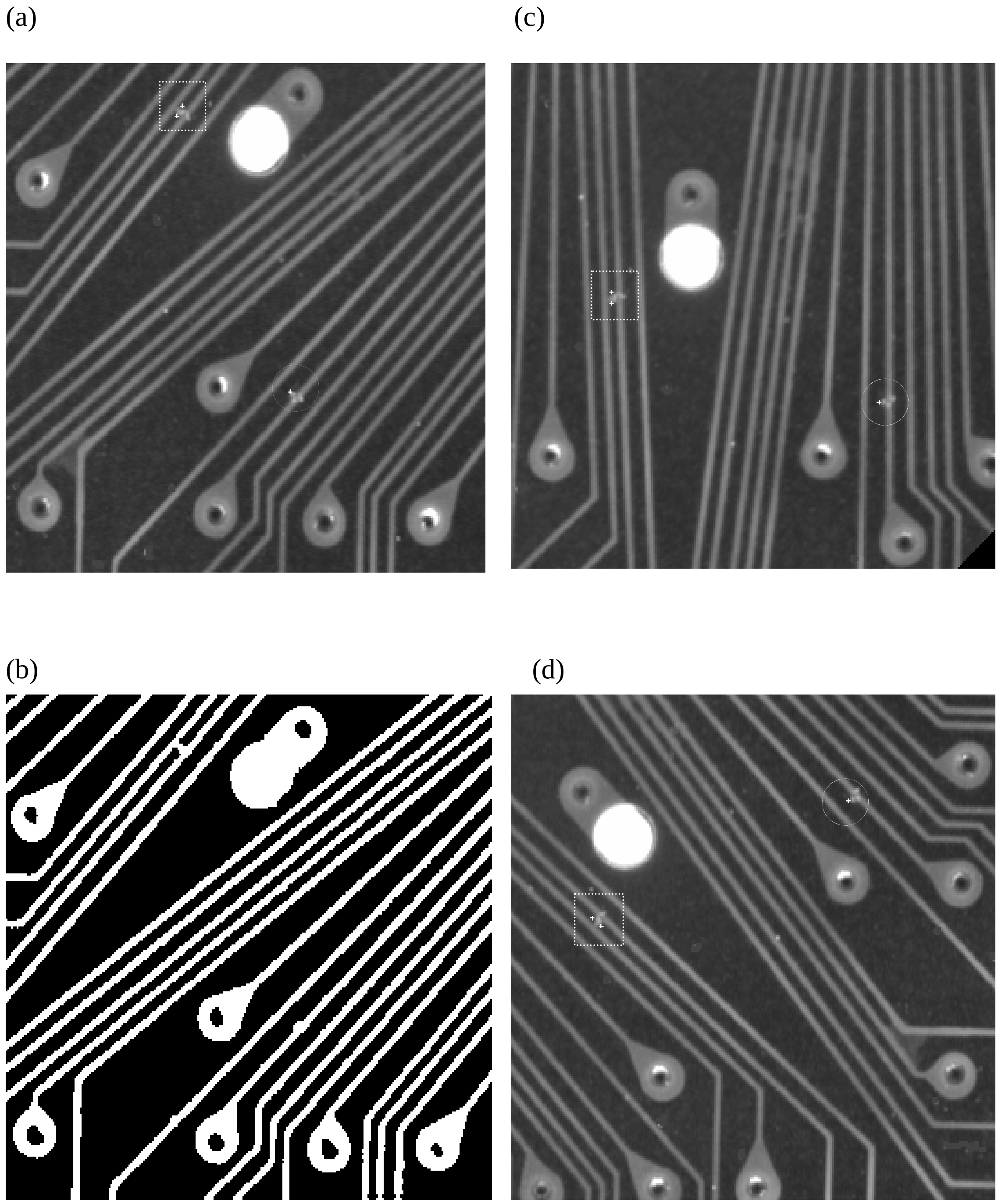

Fig. 11. (a) Real defective BGA substrate with a short and a spur. (b) The binary image of Fig. 11(a). (c) The image of Fig. 11(a) in 45°orientation. (d) The image of Fig.11(a) in 90°orientation. (The short and spur defects are respectively marked by white squares and circles dotted lines.)

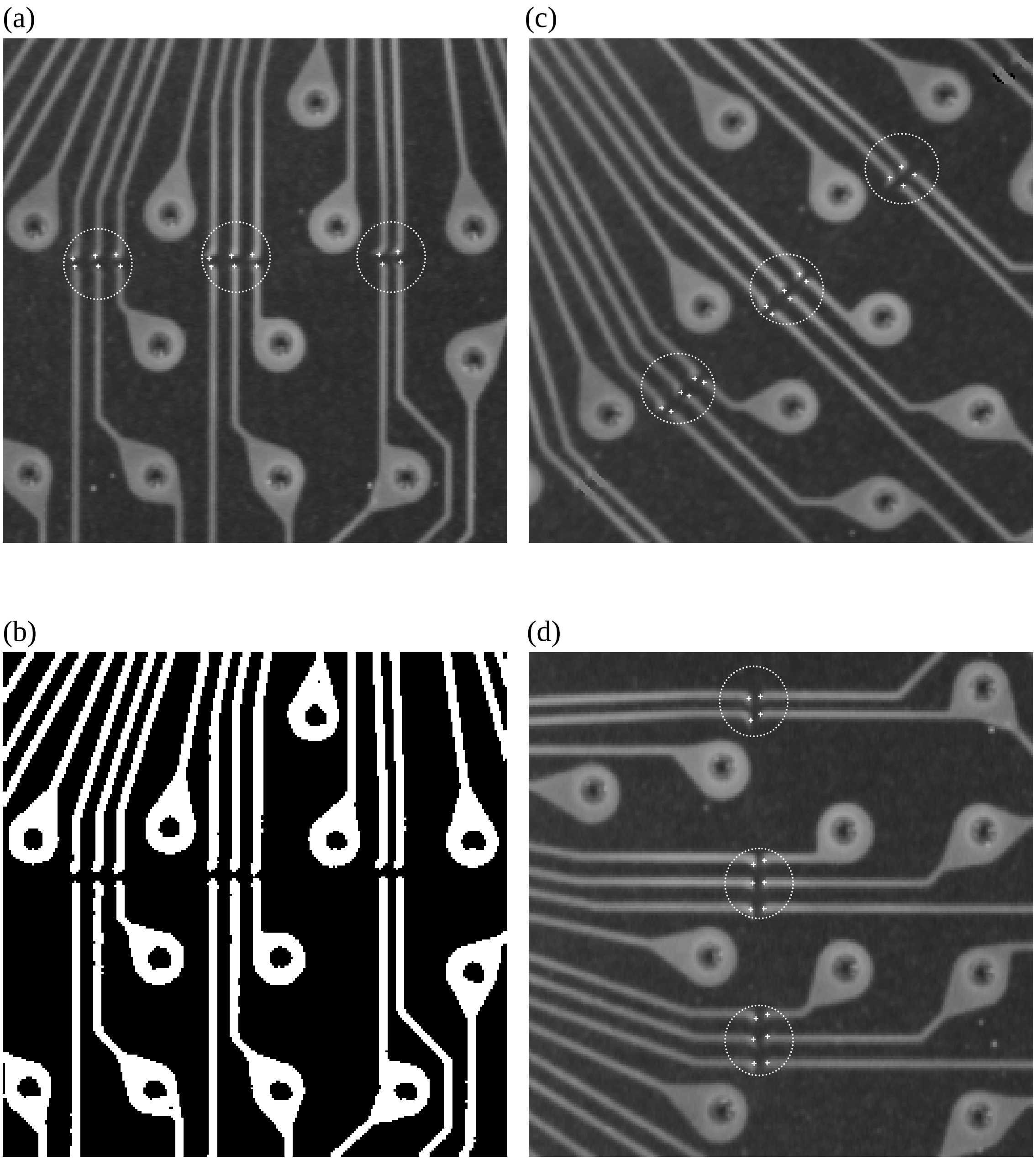

Fig. 12. (a) Real defective BGA substrate with open defects. (b) The binary image of Fig. 12(a). (c) The image of Fig. 12(a) in 45°orientation. (d) The image of Fig.12(a) in 90°orientation. (The open defects are encircled by white dotted lines)

5. Conclusion

In this study, the BGA substrate conduct path boundary defects such as open, short, mousebite, and spur have been detected by a wavelet-based approach. The 2-D boundaries of BGA substrate conduct paths are initially transformed in the 1-D $\boldsymbol{\theta}$-$\boldsymbol{s}$ representation, which is based on the eigenvetors of the covariance matrix of the boundary points over a small region. Then, the 1-D $\boldsymbol{\theta}$-$\boldsymbol{s}$ representation is decomposed by the MRD in wavelet function to locate the boundary defect candidates. Further, true defects can be identified among the potential defective regions by evaluating their energy and correlation coefficients with a golden data set. The proposed approach avoids inspection errors resulting from board distortion and misalignment. It requires no pre-stored templates, no template-matching procedure, and no training process. Therefore, computational time and data storage can be significantly reduced. With the decomposition levels greater than 3 in MRD, the proposed method is rotation-invariant and can achieve 100% correct detection for the boundary defects on BGA substrates conduct paths by using the wavelet bases with appropriate support length such as s4, d4, or c6 at $\boldsymbol{D}_1$ scale.

References

1. N. Chandler and S. G. Tyler, "Ultra-fine feature printed circuits and multi-chip Modules", Microelectronics Journal, 26 (4), pp. 393-404, 1995.

2. U. D. Perera, "Evaluation of reliability of μBGA solder joints through twisting and bending", Microelectronics Reliability, 39 (3), pp. 391-399, 1999.

3. M. Mogant, F. Ercal, "Automatic PCB inspection algorithms: a survey", Computer Vision and Image Understanding, 63 (2), pp.287-313, 1996.

4. Y. Hara, N. Akiyama, and K. Karasaki, "Automatic inspection system for printed circuit boards", IEEE Transactions on Pattern Analysis and Machine Intelligence, 5 (6), pp. 623-630, 1983.

5. T. Pavlidis, "Minimum storage boundary tracing algorithm and its application to automatic inspection", IEEE Transactions on Systems, Man, and Cybernetics, SMC-8, pp. 66-69, 1978.

6. W. Y. Wu, M. J. Wang, and C. M. Liu, "Automated inspection of printed circuit boards through machine vision", Computer in Industry, 28 (2), pp. 103-111, 1996.

7. G. A. W. West, "A system for the automatic visual inspection of bare-printed circuit Boards", IEEE Transactions on Systems, Man, and Cybernetics, 14 (5), pp. 767-773, 1984.

8. W. M. Sterling, "Automatic non-reference inspection of printed wiring boards", Proceeding IEEE Computer Society Conference Pattern Recognition and Image Processing, pp. 93-100, August 1979.

9. J. W. Foster III, P. M. Griffin, J. R. Villalobos, and S. L. Messimer, "Automated visual inspection of bare printed circuit boards", Computer Industry Engineering, 18 (4), pp. 505-509, 1990.

10. H. Tsunekawa, "Latest image evaluation systems aid efforts for product quality", Journal of Electronic Engineering, 29 (306), pp. 72-77, 1992.

11. J. R. Mandeville, "Novel method for analysis of printed circuit images", IBM Journal Research and Development, 29 (1), pp.73-87, 1985.

12. M. Mogant, and F. Ercal, "Segmentation of printed circuit board images into basic Patterns", Computer Vison and Image Understanding, 70 (1), pp. 74-86, 1998.

13. M. Mogant, and F. Ercal, "A subpattern level inspection system for printed circuit Board", Computer Vison and Image Understanding, 70 (1), pp. 51-62, 1998.

14. T. F. Cootes, G.J. Page, C. B. Jackson, and C. J. Taylor, "Statistical grey-level models for object location and identification", Image and Vision Computing, 14 (8), pp. 533-540, 1996.

15. C. K. Chui, An introduction to wavelets, Academic Press, Boston, 1992.

16. I. Daubechies, Ten lectures on wavelets, SIAM, Philadelpha, 1992.

17. I. Daubechies, "The wavelets transform. Time-frequency localization and signal analysis ", IEEE Transaction on Information Theory, Vol. 36, No. 5, pp. 961-1005, 1990.

18. G. Y. Chen and T. D. Bui, "Invariant Fourier-wavelet descriptor for pattern recognition", Pattern Recognition, Vol. 32, pp. 1083-1087, 1999.

19. B. Y. Lee and Y. S. Tarng, "Application of the Discrete Wavelet Transform to the Monitoring of Tool Failure in End Milling Using the Spindle Motor Current", International Journal of Advanced Manufacturing Technology, Vol. 15, pp. 238-243, 1999.

20. A. Bruce and H. Y. Gao, Applied Wavelet Analysis with S-PLUS, Springer-Verlag, New York, 1996.

21. J. S. Lee, Y. N. Sun, and C. T. Tsai, "Wavelet based corner detection", Pattern Recognition, Vol. 26, No. 6, pp. 853-865, 1993.

22. J. S. Lee, Y. N. Sun, and C. T. Tsai, "Multiscale Corner Detection by Using Wavelet Trans-Formation", IEEE Transactions on Image Processing, Vol. 4, No. 1, pp. 100-104, 1995.

23. A. Quddus and M. M. Fahmy, " Fast wavelet-based corner detection technique", Electronics Letters. Vol. 35, No. 4, 1999.

24. M. C. Fairhurst, Computer Vision for Robotic Systems: An Introduction, Prentice Hall, Englewood Cliffs, NJ, 1988.

25. D. M. Tsai, H. T. Hou, and H. J. Su, "Boundary-based corner detection using eigenvalues of covariance matrices", Pattern Recognition Letters, 20, pp. 31-40, 1999.

26. R. C. Gonzalez and R. E. Woods, Digital Image Processing, Addison Wesley, Massaschusetts, 1993.